TECHNICAL UNIVERSITY OF CLUJ-NAPOCA

ACTA TECHNICA NAPOCENSIS

Series: Applied Mathematics, Mechanics, and Engineering
Vol.67, Issue IV, November, 2024

ANALYSIS OF THE THERMAL EXPANSION COEFFICIENT OF ANISOTROPIC SOLIDS: APPLICATION TO CALCIUM SILICATE – PART I – INTRODUCTION TO MEASUREMENT METHODOLOGY

Adrian-Ioan BOTEAN

Abstract: *This paper aims determining the linear thermal expansion coefficient (CTE) of calcium silicate using an optical method for measuring deformations called digital image correlation method (DIC). DIC provides full-field in-plane deformation fields of the test planar specimen surface by comparing the digital images of the specimen surface acquired before and after deformation. The samples evaluated in this paper are two calcium silicate plates: a square one (with sides of 50x50 mm and 3 mm of thickness) and a circular one (with a diameter of 50 mm and a thickness of 3 mm). The measuring set-up developed includes a simple heating device, thermal sensors and a thermo-camera for real-time temperature measurement and monitoring of the sample and a 2D and 3D-DIC measuring system. The study is carried out during two stages: Part I – Introduction to the measurement methodology and Part II – Evaluation of the experimental data.*

Key words: *thermal expansion coefficient (CTE), thermal displacement, calcium silicate, digital image correlation (DIC).*

1. INTRODUCTION

In this study, we aim to determine the linear thermal expansion coefficient (CTE) of the calcium silicate (Ca_2SiO_4). For this study, calcium silicate has the following typical parameters: Chemical Composition (%): SiO_2 37-42, CaO 29-34, Al_2O_3 10-12, MgO 1.8-2.1; Density (kg/m^3) 230±10%; Tensile Stresses (MPa) ≥0.30; Compressive Stresses (MPa) ≥0.50; Thermal Conductivity (W/m·K): 100°C≤0.057, 200°C≤0.069, 400°C≤0.098.

The thermal expansion of materials from the calcium silicate family is known to be highly anisotropic [1-4]. Such anisotropy can cause large thermal stresses and subsequent microcracks in polycrystalline materials with randomly oriented grains. The thermal expansion coefficient and the microscopic thermal stresses of calcium silicate depend on its microstructural composition and the internal relative humidity.

However, the elastic anisotropy of these materials is generally unknown; furthermore, it is more difficult to determine experimentally than the anisotropy of the CTE. The technique for measuring CTE proposed in this study is based on digital image correlation (DIC) method.

The work discusses the CTE calculation of anisotropic materials, influence of a small rigid body rotation and analyses the accuracy of strain calculation procedure. In the first part the DIC procedure is explained and the experimental set-up is outlined. The noise contained in the calculated displacements, especially when small displacements are measured, will be amplified if the strains are calculated by numerical differentiation of the displacement field. The possibilities to get more precise and reliable strain results are discussed in the paper. An assessment of the error on the obtained CTE is made at the end of the paper.

Microporous calcium silicate is one of the best lightweightlated construction inorganic thermal insulation materials for high temperature uses. The general formula of calcium silicate has the following chemical

Received: 25.08.24; **Similarities**: 24.11.24: **Reviewed**: 05.11./07.11.24: **Accepted**:25.11.24.

expression: $xCaOySiO_2zH_2$, where x, y, and z are coefficients whose size can vary depending on the concentrations of the chemical components. Thus, the amount of calcium oxide must be between 3% and 35%, and that of silica between 50% and 95%, these amounts are measured in weight on a dry basis. It can be anhydrous, i.e. value that z receives is 0 or hydrates. Calcium silicate is widely used in many different industries and applications: Construction industry, in which case calcium silicate is used as insulation material, fireproofing agent, and refractory material - according to Figure 1 [5-10]. In electrotechnical industry for insulation of PVC cables and high voltage equipment (Figure 2) - calcium silicate bearing the name of Wollastone with crystalline form and having the chemical composition $CaSiO_3$ [12, 13].

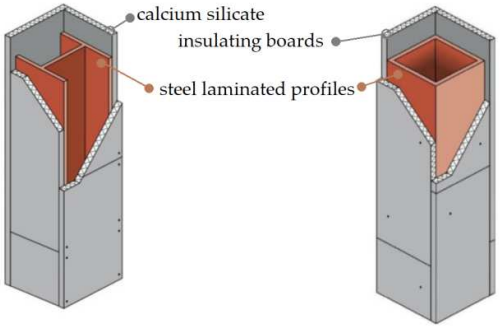

Fig. 1. Calcium silicate boards used for fire-resistant insulation of metal structures [11].

Fig. 2. Calcium silicate used to insulate PVC pipes [14].

In the medical field: being composed of tricalcium silicate, dicalcium silicate, calcium carbonate and zirconium oxide, biodentine is a bioactive cement with low porosity and a higher mechanical hardness compared to other materials, this makes it similar to dentine. When the three carbon silicates are mixed with water, they form a sticky hydrate gel that will solidify in a very short time, thus forming a hard structure. This accelerates the formation of bridges in the dentin, having a positive effect on the cells of the dental pulp as can be seen in Figure 3 and 4 [15-18].

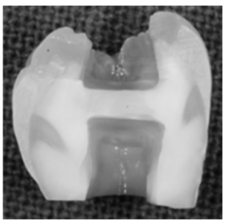

Fig. 3. Pulp chamber without Ca_2SiO_4 [15].

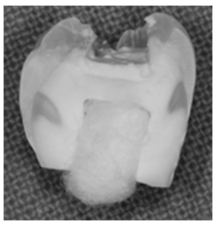

Fig. 4. Pulp chamber with Ca_2SiO_4 [15].

In the 90s, calcium silicate ceramics began to be tested as biomaterials. This, having a superior bioactivity compared to other materials, has been studied to be used in the regeneration of bone tissue. Because it contains silicon and has a high resistance to mass, resistance to corrosion, calcium silicate ceramic has an essential role in the various mechanisms that lead to the formation of new bone. In the absence of bone tissue, the calcium silicate composition is added, this being covered with a membrane so that the implant can be made later, the calcium silicate being the substitute for the bone tissue. Calcium silicate-based materials represent a very important class of bioactive materials for their use in bone regeneration [19-22].

Thermal expansion and thermal conductivity are two common thermal properties [23-27]. Thermal expansion is the tendency of matter to change in volume in response to a change in temperature. In practice, linear coefficient of thermal expansion (CTE) is generally used to characterize the thermal expansion of a material, which measures the fractional change in length per degree change in temperature at a constant pressure [28, 29].

Thermal and mechanical stability are of crucial importance in development of lightweight composite structures [30-32]. It should be emphasized that extreme temperature operating environments are not unusual in numerous different applications, where temperatures have been estimated to vary between -180 ^{0}C and +500 ^{0}C. Dimensional

stability of structural materials operating under such conditions is only possible if this have very low thermal expansion properties [33-35]. A large positive thermal expansion (PTE) is useful in thermal actuators and medical vessel dilators that operate based on human body temperature [36-38]. A negative thermal expansion (NTE) is useful for cancelling the thermal expansion of ordinary materials in high – temperature or high – precision devices [39-43].

The determination of the coefficient of linear thermal expansion can be achieved by means of a wide variety of experimental techniques: volumetric method [44, 45], dilatometry and laser flash [28, 46-49], X-ray diffraction [50-52], electrical resistance strain gages [53, 54]. These techniques need specific sample preparation that can bring in errors (sample cutting, gauge gluing ...) and only give information at the specimen scale.

In this paper, an alternative technique for non-contact full-field deformation measurement, namely, the digital image correlation (DIC) technique [55–60] is proposed to determine the CTE of calcium silicate. DIC offers the following advantages: relative simple experimental set-up and specimen preparation; low environmental vulnerability (vibration); flexible measurement sensitivity and adjustable spatial resolution; no limits on the temperatures and strains than can be reached; easy and automatic data processing.

2. MATERIALS AND METHODS

DIC provides full-field in-plane deformation fields of the test planar specimen surface by comparing the digital images of the specimen surface acquired before and after deformation.
In practical implementation of DIC, a region of interest (ROI) in the reference image is specified first and divided into evenly spaced virtual grids. If this calculation is done for every point of the object surface, the 3D surface contour of the object can be determined in all areas, which are observed by both cameras. A series of measurements is taken, while the specimen surface is moved due to a loading, the displacements are computed at each point of the virtual grids to obtain the full-field deformation.

The basic principle of DIC is schematically illustrated in Figure 5, where it is shown the reference square subset (reference image) and target subset (deformed image), the differences of positions of the reference subset center and target subset center yield in-plane displacement components u and v. Target subset can have different shapes or positions (a_o ... a_3, b_o ... b_3) named pseudo-affine transformation.

Random gray value dot patterns (Stochastic Pattern – SP) on specimen surfaces (Measurement Surface – MS) are observed by two CCD cameras from different directions in a stereoscopic setup [61, 62], the position of each object point being focused on a specific pixel in the camera plane.

Knowing the imaging parameters for each camera and the orientations of the cameras with respect to each other, the displacement components of the reference and target subset centers can be calculated.

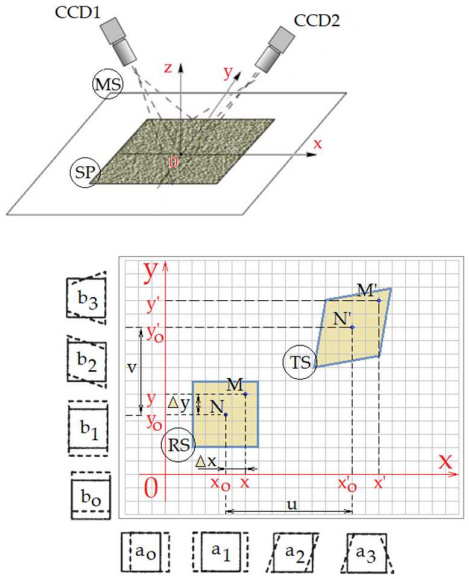

Fig. 5. Schematic figure of 3D-DIC principle.
MS – Measurement Surface, **SP** – Stochastic Pattern, **RS** – Reference subset, TS – Target Subset.

To obtain accurate estimation for the displacement components of the same point in the reference and deformed images is used Zero Mean Normalized Cross-Correlation or shorter ZNCC and is an integer you can get when you compare two grayscale images.

A square reference subset of (2n+1)x(2n+1) pixels (typically a facet size between 20x20 and 30x30 pixels is chosen) centered at the current

Received: 25.08.24; **Similarities**: 24.11.24: **Reviewed**: 05.11./07.11.24: **Accepted**:25.11.24.

point $N(x_o,y_o)$ from the reference image is chosen and used to find its corresponding location in the deformed image (according to Figure 5) – point $N'(x_o',y_o')$.

For reference subset and target subset the sum of squared differences (SSD) are expressed by relation:

$$\mathrm{SSD}(\mathrm{Img}_1,\mathrm{Img}_2,x_o,y_o,x_o',y_o',n)=\sum_{i=-n}^{n}\sum_{j=-n}^{n}[\mathrm{Img}_1(x_o+i,y_o+j)-\mathrm{Img}_2(x_o'+i,y_o'+j)]^2 \quad (1)$$

When the sum of squared differences is zero the reference subset is identical with target subset, and the sum of squared differences are small values the target subset is deformed.

The gray level intensity at coordinates (x_o,y_o) in the reference subset of the reference image is $\mathrm{Img}_1(x_o,\ y_o)$ and the gray level intensity at coordinates (x_o',y_o') in the target subset of the deformed image is $\mathrm{Img}_2(x_o',y_o')$. The average gray value intensity of reference and target subsets are expressed by:

$$\mathrm{Img}_1(x_o,y_o)_m=\frac{1}{(2\cdot n+1)^2}\cdot\sum_{i=-n}^{n}\sum_{j=-n}^{n}\mathrm{Img}_1(x_o+i,y_o+j) \quad (2)$$

$$\mathrm{Img}_2(x_o',y_o')_m=\frac{1}{(2\cdot n+1)^2}\cdot\sum_{i=-n}^{n}\sum_{j=-n}^{n}\mathrm{Img}_2(x_o'+i,y_o'+j) \quad (3)$$

The average gray value is:

$$\overline{Img}(u,v,n)=\frac{1}{(2\cdot n+1)^2}\cdot\sum_{i=-n}^{n}\sum_{j=-n}^{n}Img(u+i,v+j) \quad (4)$$

The Zero Mean Normalized Cross-Correlation (to evaluate the similarity in reference and target subsets) is defined as:

$$ZMNCC_{Img_1,Img_2}(u,v,x_o,y_o,x_o',y_o')=$$

$$=\sum_{i=-n}^{n}\sum_{j=-n}^{n}\left[\frac{\mathrm{Img}_1(x_o,y_o)-\mathrm{Img}_1(x_o,y_o)_m}{\sqrt{\sum_{i=-n}^{n}\sum_{j=-n}^{n}[\mathrm{Img}_1(x_o,y_o)-\mathrm{Img}_1(x_o,y_o)_m]^2}}-\frac{\mathrm{Img}_2(x_o',y_o')-\mathrm{Img}_2(x_o',y_o')_m}{\sqrt{\sum_{i=-n}^{n}\sum_{j=-n}^{n}[\mathrm{Img}_2(x_o',y_o')-\mathrm{Img}_2(x_o',y_o')_m]^2}}\right]^2 \quad (5)$$

If the subset is small enough each points M(x,y) around the subset center $N(x_o,y_o)$ in the reference subset can be mapped to point $M'(x',y')$ in the target subset according to the following displacement mapping function:

$$M'(x',y')=M'\left(x_o+\Delta x+u+u_x\cdot\Delta x+u_y\cdot\Delta y,\ y_o+\Delta y+v+v_x\cdot\Delta x+v_y\cdot\Delta y\right) \quad (6)$$

u_x, u_y, v_x, v_y are the displacement gradient components for the subset; u, v are the displacement components for the subset center N in the x and y directions respectively; the terms Δx, Δy are the distance from the subset center N to point M.

The correlation function can be optimized using the iterative correlation algorithm to resolve the deformation parameters. The correlation algorithm is based on a pseudo-affine coordinate transformation (Figure 1: a_o-a_3 and b_o-b_3 - translations, stretch, shear and distortion) from one camera image to another:

$$x'=a_o+a_1\cdot x+a_2\cdot y+a_3\cdot x\cdot y \quad (7)$$

$$y'=b_o+b_1\cdot x+b_2\cdot y+b_3\cdot x\cdot y \quad (8)$$

Small rigid body translation and rotation can occur during the thermal expansion of the test specimen. Absolute thermal expansion cannot be obtained directly, because the displacements computed by the DIC technique also contain the displacements caused by rigid body translation and rotation. The displacements associated with the rigid body rotation are much larger than that

caused by thermal expansion. To remove the influence of the rigid body translation and rotation, a new coordinate system as illustrated in Figure 6 with its origin point located in the calculation area's center is introduced.

The influence of rigid body translation can be eliminated by subtracting the displacements of the calculation area center points. It is easy to remove the influence of small rigid body rotation under the condition that the rotation angle can be accurately determined.

Assume the test specimen rotates anti-clock wisely with angle of Δβ during thermal expansion, as shown in Figure 6.

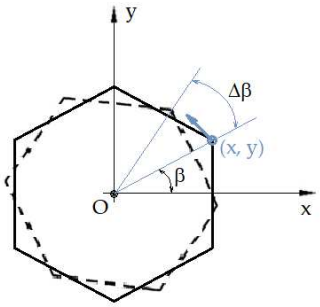

Fig. 6. Diagram of the influence of small rigid body rotation on the displacement of point (x, y).

The displacement components of current point (x, y) can be rewritten as:

$$u(x,y) = \alpha_x \cdot x \cdot \Delta t - y \cdot \Delta\beta \quad (9)$$

$$v(x,y) = \alpha_y \cdot y \cdot \Delta t + x \cdot \Delta\beta \quad (10)$$

where α_x and α_y are the CTE values to be determined [57].

For isotropic materials:

$$\alpha_x = \alpha_y \quad (11)$$

For anisotropic materials:

$$\alpha_x \neq \alpha_y \quad (12)$$

because the anisotropic materials [1-4] usually undergoes non-uniform thermal expansion. [57]

The displacement fields u(x, y), v(x, y) are affected by the small rigid body rotation of the considered specimen during thermal expansion. For this reason, the contour lines of u or v displacement field will no longer be parallel with the x or y axis if small rigid body rotation of the calcium silicate specimen occurs during thermal expansion.

For small deformations, the rigid body rotation angle Δβ can be calculated with the relation:

$$\Delta\beta = \frac{1}{2} \cdot \left(\frac{\partial v}{\partial y} - \frac{\partial u}{\partial x}\right) \quad (13)$$

The rigid body motions are assumed to be small and they can be easily removed from the DIC procedure by subtracting the displacements of the calculation area centre points.

The samples evaluated in this paper are two calcium silicate plates: a square one (with sides of 50x50 mm and 3 mm of thickness) and a circular one (with a diameter of 50 mm and a thickness of 3 mm).

For measurements a random speckle pattern on the surface of the target specimens is necessary. The pattern was produced by black spray applied on an initial painted matt white grounding specimen surface (Figure 7).

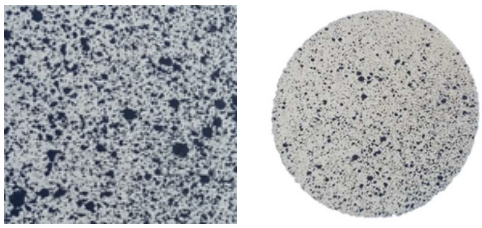

Fig. 7. The pattern on the surface of the target specimens.

These plates are heated at the level of the facet opposite to the one on which the random speckle pattern is generated.

In the case of measuring the CTE by DIC it is essential that there are no mechanical constraints, either internal or external on the target specimens so that no stresses occur in the body during thermal expansion or contraction. For this reason, a cube and an aluminum cylinder were processed on which the two plates considered for the study will be placed freely (Figure 8).

Both in the cylinder and in the cube, a hole with a diameter of 12 mm and a depth of 25 mm is machined into which the electrode of a heating system that works on the basis of the Joule-Lenz effect and which can generate a temperature of up to 500 degrees Celsius (Figure 9).

The heating stand (Figure 10) is composed of a support plate (steel), reference E, on which the electrode B is fixed through a magnetic support (reference D). The intermediate element for stiffening the electrode - reference C, was designed using the SolidWork program and 3D

Received: 25.08.24; **Similarities**: 24.11.24: **Reviewed**: 05.11./07.11.24: **Accepted**:25.11.24.

printed using the ZORTRAX M200 3D printer with Z-Filament Series: Z-Ultrat, Ivory.

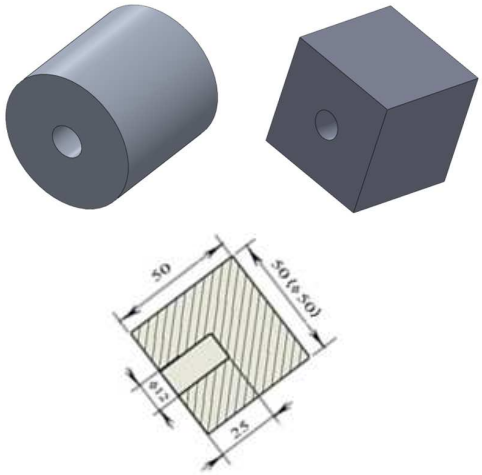

Fig. 8. Cube and an aluminum cylinder design.

Fig. 9. Heating system by Joule – Lenz effect. **B** – electrode.

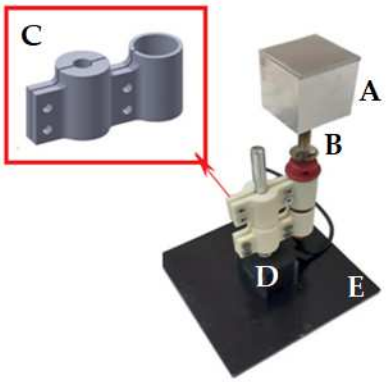

Fig. 10. The stand for heating calcium silicate samples:
A - aluminum cube, **B** - heating electrode, **C** - electrode stabilization element, **D** - magnetic support, **E** - steel support plate.

The calcium silicate plates are positioned on the aluminum cube or cylinder (reference A in Figure 10) and are heated according to Figure 11.

For the initial state (I.S.) the temperature on both sides is equal to the ambient temperature t_1. As the lower side registers an increase in temperature (t_2), on the upper side the temperature is $t_2' < t_2$ ($t_2' > t_1$) corresponding to a final state of heating (F.S.).

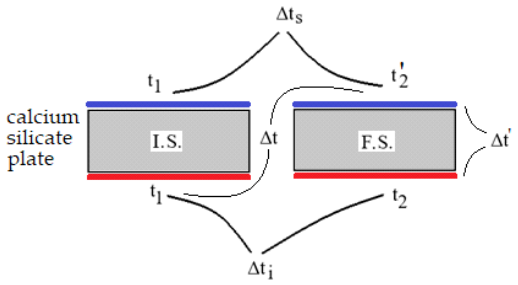

Fig. 11. Distribution of temperatures in the calcium silicate plate for the initial state (I.S.) and the final state (F.S.) of heating:
t_1 – the temperature of the lower and upper facets for the initial state of heating (equal to the ambient temperature); **t_2** – temperature of the lower facet for the final state of heating; **t_2'** – temperature of the upper face for the final state of heating; **Δt_s**- the temperature gradient at the level of the upper face corresponding to the final and initial state of heating; **Δt_i -** the temperature gradient at the level of the lower face corresponding to the final and initial state of heating; **$\Delta t'$** – the temperature gradient between the lower and the upper facet for the final state of heating; **Δt** – the temperature gradient between the lower side corresponding to the initial state of heating and the upper side corresponding to the final state of heating.

The temperature gradient at the level of the upper face corresponding to the final and initial state of heating (Δt_s) is expressed through the following relationship:

$$\Delta t_s = t_2' - t_1 \quad (14)$$

The temperature gradient at the level of the lower face corresponding to the final and initial state of heating (Δt_i) is:

$$\Delta t_i = t_2 - t_1 \quad (15)$$

The temperature gradient between the lower and the upper facet for the final state of heating ($\Delta t'$) is expressed through the following relationship:

$$\Delta t' = t_2 - t_2' \quad (16)$$

The temperature gradient between the lower side corresponding to the initial state of heating and the upper side corresponding to the final state of heating (Δt) is:

$$\Delta t = t_2' - t_1 \quad (17)$$

Monitoring the temperature of the upper face of the calcium silicate plates, in real time, is done with a FLIR T400 thermal imaging camera as shown in Figure 12. It is an infrared camera

that allows direct superimposition over the corresponding visible image. This functionality combines the benefits of both infrared and visual imaging. The image quality is extremely clear as it offers a resolution of 320x240 pixels. The T400 offers both autofocus and manual focus with a continuous 8x zoom. It can register high temperatures up to 1,200 °C, having a thermal sensitivity of 0.05 °C.

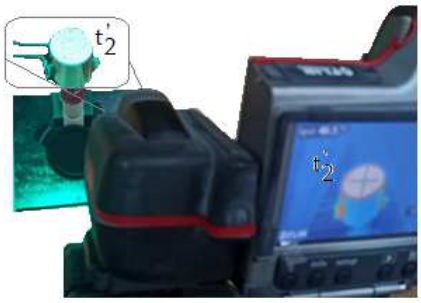

Fig. 12. Real – time monitoring of calcium silicate plate with T400 thermal imaging camera.

At the level of the lower facet, the temperature is measured, in real time, with two Pt100 thermoresistances glued to the upper part of the cylinder, respectively of the aluminum cube (Figure 13).

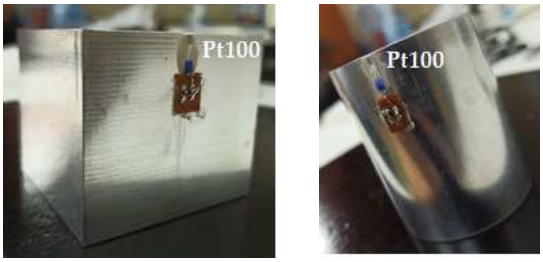

Fig. 13. Thermistor Pt100 soldered on the heating elements (cube and cylinder) of the calcium silicate plates.

Pt100 connects to the Spider 8 data acquisition system (HBM) and the data is viewed, in real time, using the CatmanEasy software (HBM) as shown in Figure 14. The temperature (t_2) measurement frequency is 5 Hz.

The thermal expansion in plane (2D) or out of plane (3D) is measured with the Q400 digital correlation system from Dantec Dynamics (www.dantecdynamics.com), that includes two CCD cameras, 1/8", 1624x1234 pixel resolution, frame rate up to 30 Hz, electronic control, lenses with 17 mm focal length and patented cold light system HILIS (High Intensity LED Illumination System) for very homogenous illumination of the specimen [61].

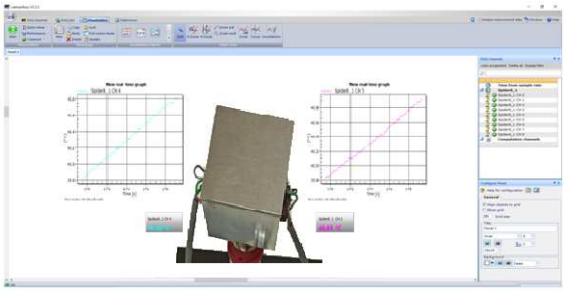

Fig. 14. CatmanEasy software interface configured for t_2 temperature measurement.

Before any measurement in case of 2D or 3D-DIC a system calibration is necessary to be performed. The system calibration is needed for transforming image positions on the CCDs of the two cameras of a specimen surface point to the corresponding 3D coordinates of that point. Calibration errors are potentially a major source of systematic evaluation errors, limiting the resolution of the results. The Q400 system has, for a successful measurement, a calibration procedure incorporated in the measurement and analysis software (Isra4d Software). To determine the intrinsec parameters, a calibration plate, according to Figure 15, is used, which is rotated and translated manually in front of the CCD cameras.

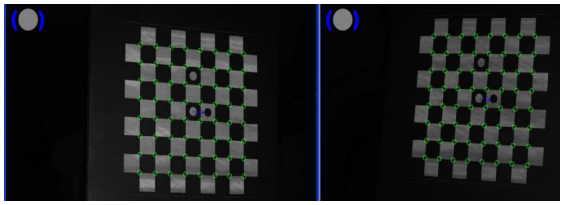

Fig. 15. Determining the intrinsec and extrinsec parameters of CCD cameras using the calibration plate.

The Isra4D software automatically records the nodal points of the calibration plate in a sequence of images and calculates intrinsec and extrinsec parameters (Figure 16).

Thus, the intrinsec CCD camera 1 parameters are: focal length (x; y) 3798±6; 3797±7, principal point (x; y) 705±13; 488±7, radial distortion (r^2 ; r^4) -0.171±0.017; - 2.2±1.0, tangential distorsion (t_x; t_y) -0.0003±0.0003;

Received: 25.08.24; **Similarities**: 24.11.24: **Reviewed**: 05.11./07.11.24: **Accepted**:25.11.24.

0.0011±0.0005 and for CCD camera 2 are: focal length (x; y) 3813±7; 3810±7, principal point (x; y) 716±13; 492±8, radial distortion (r^2 ; r^4) -0.210±0.012; -0.50±0.15, tangential distorsion (t_x; t_y) -0.0011±0.0003; 0.0004±0.0010.

Extrinsec parameters are represented by the translation vector and the rotation matrix. Thus, the extrinsec parameters for CCD camera 1 are: rotation vector (x; y; z) -2.006±0.002; 2.0256±0.0017; - 0.567±0.003, translation vector (x; y; z) -6.1±1.3; 2.2±0.7; 387.2±0.7 and for CCD camera 2 are: rotation vector (x; y; z) 2.007±0.002; -1.974±0.002; -0.265±0.004, translation vector (x; y; z) -40.3±1.4; -3.2±0.9; 414.7±0.8.

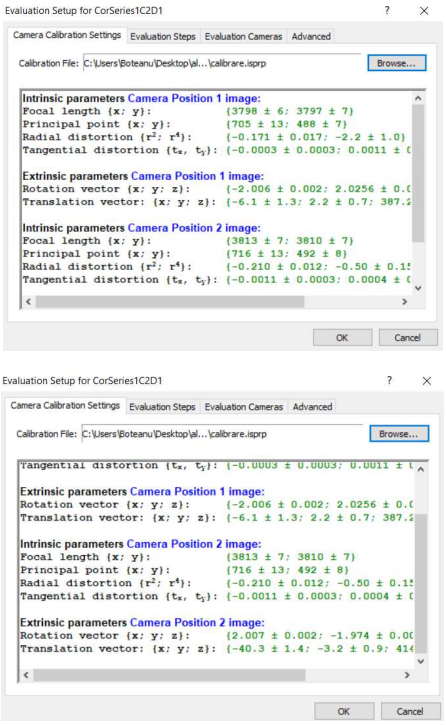

Fig. 16. The intrinsec and extrinsec parameters of CCD1 and CCD2 cameras.

DIC reconstruct displacements with subpixel accuracy and tangential surface strains in the μstrain range. For large deformations (>1%) DIC is especially suitable. According to the tests performed by the producer of Q400 system [61, 63, 64] the displacement errors are present in the order of less than 0.02 pixels, strain errors are limited to 0.2 mm/m when using a lens with 17 mm focal length. If present displacements are small (lower than 50 pixels), the errors scale linearly. Relative displacement errors are in the order of 0.01-0.05%, strain errors typically count 1-5 με/pixel, related to the existent displacements [61, 63, 64].

In the applications presented here the gray value interpolation is bicubic spline, correlation accuracy has a value of 0.1 pixels, correlation residuum is 20 and 3D reconstruction residuum is 0.4 pixels. For the circular model, the number of subset references in the x direction (in accordance with the diameter) is 31 and in the y direction (in accordance with the diameter) is 29. Since the facet (reference subset) size is 17 pixels, it follows that in relation to the x axis the reference subset sum is 527 pixels (10.54 pixels/mm) and in relation to the y axis the reference subset sum is 493 pixels (9.86 pixels/mm). For the rectangular model, the number of subset references in the x direction (in accordance with the diameter) is 28 and in the y direction (in accordance with the diameter) is 26. Since the facet (reference subset) size is 17 pixels, it follows that in relation to the x axis the reference subset sum is 476 pixels (9.52 pixels/mm) and in relation to the y axis the reference subset sum is 442 pixels (8.84 pixels/mm)

The size of the displacements in this study, in relation to the x (denoted dx) and y (denoted dy) axes corresponding to the xOy plane (according to Figure 5) but also out of plane (denoted dz) are below 1%. For this reason, measured strains are typically accompanied by a large amount of noise. If the strains are calculated by differentiating the displacement field, the numerical differentiation will amplify the noise contained in the calculated displacements. One possibility to solve this problem is to average the measured strains over a large area where the strain distribution is supposed to be homogeneous. A better result can be obtained calculating in-plane Green-Lagrange strain components by the analysis of the distortion of each local facet as mentioned above [61, 62] or simply use linear planes to approximate the computed displacement field [57].

For anisotropic materials, CTE in relation to the x and y axes normally doesn't equal to CTE in relation to the z axis because the anisotropic materials usually undergo non-uniform thermal expansion.

The displacement fields dx, dy and dz are affected by the small rigid body rotation of the calcium silicate specimen during thermal expansion. For this reason, the Remove rigid body movements option is activated in the Isra 4D software.

In Figure 17, the displacements in relation to the x axis can be visualized for the circular and square specimens in the form of a field of isocolors.

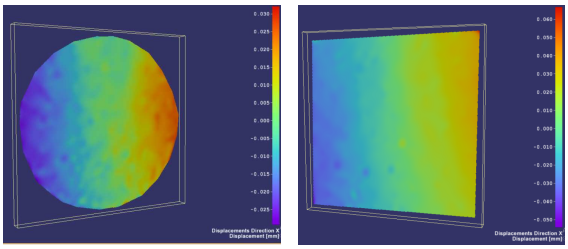

Fig. 17. Field of displacements in relation to the x axis.

The displacements in the y and z directions, for the 2 considered specimens, are presented in Figure 18 and Figure 19. From these representations it can be seen that if in the case of displacements in the direction of the x and y axes, the isochromats are arranged linearly in the case of displacement in the direction of the axis z isochromats are arranged concentrically.

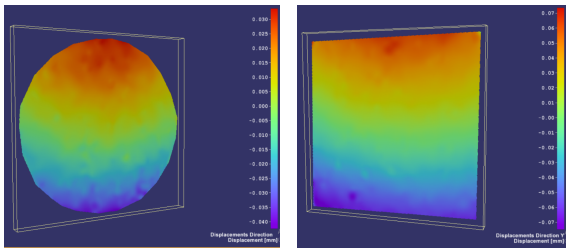

Fig. 18. Field of displacements in relation to the y axis.

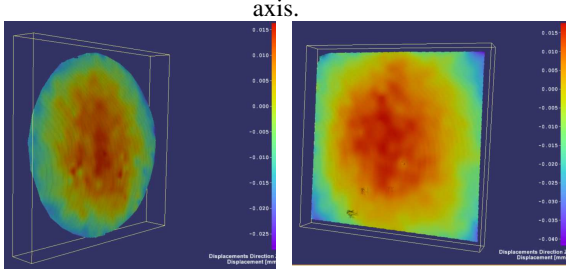

Fig. 19. Field of displacements in relation to the z axis.

The block diagram of the experimental stand can be viewed in Figure 20 and the experimental s tand in Figure 21

.

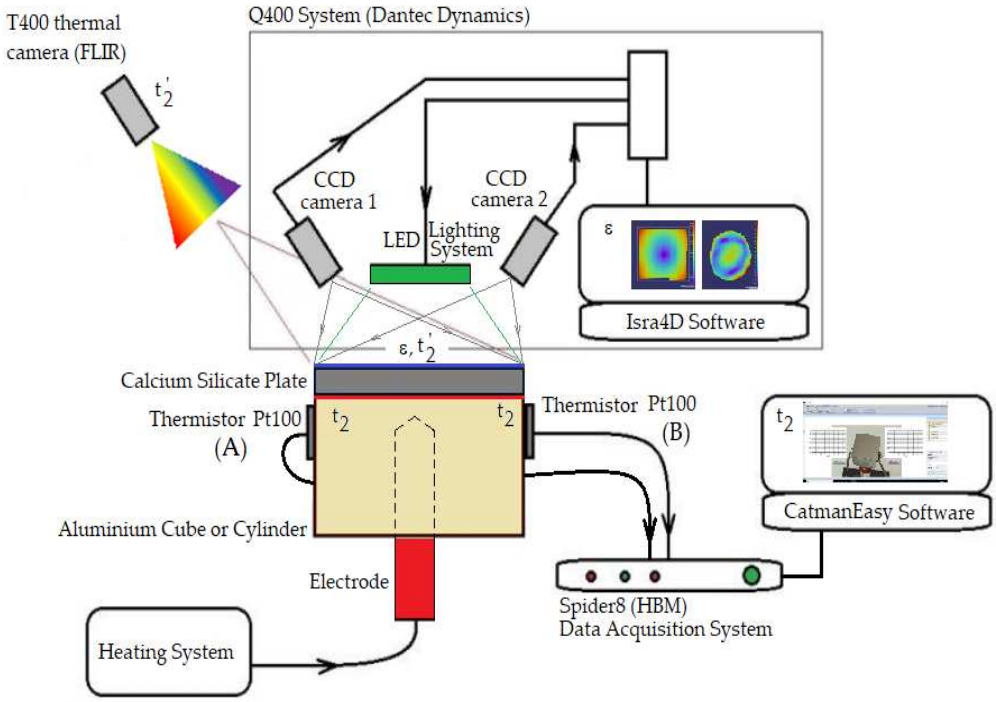

Fig. 20. Block diagram of the experimental installation.

Received: 25.08.24; **Similarities**: 24.11.24: **Reviewed**: 05.11./07.11.24: **Accepted**:25.11.24.

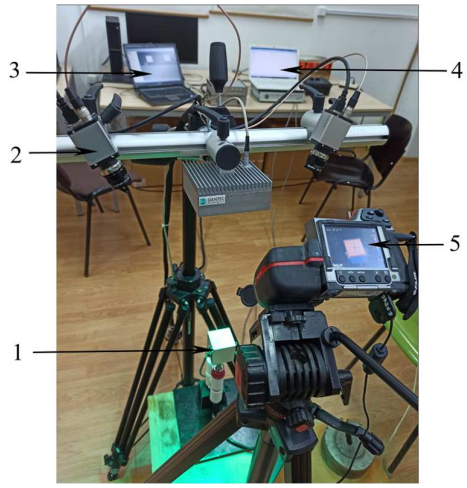

Fig. 21. Experimental installation
1. The heating system of the analyzed calcium silicate specimens; **2.** DIC Q400 System; **3.** Isra4D Software; **4.** CatmanEasy Software; **5.** T400 thermal camera.

3. CONCLUSIONS

In the initial section of the study aimed at determining the coefficient of linear thermal expansion (CTE) of calcium silicate, titled "Introduction to the Measurement Methodology," a comprehensive overview of the various applications of this material is provided. These applications span both civil construction and the medical field, showcasing the versatility and significance of calcium silicate in contemporary practices. The text delves into the fundamental concept of the linear thermal expansion coefficient, offering a detailed examination of the different experimental techniques employed to measure it effectively.

Furthermore, the principle of measuring deformations through digital image correlation (DIC) is introduced. This method is characterized by its non-contact nature, which presents both notable advantages and certain disadvantages, warranting careful consideration in its application. The text progresses by detailing the step-by-step preparation of samples, specifically focusing on the fabrication of circular and square plates. It also outlines the specialized equipment utilized in the investigative process, ensuring that readers gain a clear understanding of the methodologies involved.

The calibration of the digital image correlation system is meticulously described, along with the established measurement protocol that governs the experimentation. This careful calibration is crucial for obtaining accurate and reliable results, emphasizing the rigor involved in the study.

As a transition to the second part of this study, titled "Evaluation of Experimental Data," the focus shifts to the displacement fields observed across the entire surface of the two samples examined. These displacement fields are analyzed in relation to the reference axes x, y, and z, providing a comprehensive overview of how the materials respond to thermal expansion. This detailed exploration sets the stage for a deeper analysis of the experimental findings, contributing to the overall understanding of the material's thermal behavior.

4. REFERENCES

[1] Zheng, Q., Chung, D.O.L., *Microporous calcium silicate thermal insulator*, Mat. Sci. and Technology, Vol.6, Issue 7, 1990.

[2] Rogers, P.S., Weston, R.M., *Anisotropic properties of unidirectionally crystallized calcium metasilicate*, J. of Mat. Sci., 14, 1192-1206, 1979.

[3] Tu, Y., Shi, P., Liu, D., Wen, R., Yu, Q., Sas, G., Elfgren, L., *Mechanical properties of calcium silicate hydrate under uniaxial and biaxial strain conditions: a molecular dynamics study*, Physical Chemistry Chemical Physics, Issue 2, https://doi.org/10.1039/D1CP04474E, 2022.

[4] Ji, Q., Pellenq, R.J.-M., Van Vliet, K.J., *Comparison of computational water models for simulation of calcium-silicate-hydrate*, Computational Mat. Sci., 53, 234-240, https://doi.org/10.1016/j.commatsci. 2011.08.024, 2012.

[5] Ingham, J.P., *Geomaterials Under the Microscope*, Academic Press, ISBN 978-0-12-407230-5, https://doi.org/10.1016/C2012-0-01197-0, 2012.

[6] Georgiev, D., Bogdanov, B., Hristov, Y., Markovska, I., Angelova, K., Aidan, A.,

Building Material from Calcium Silicate – Preparation and Properties, IMS/4 Int. Conf. on the Aplications of Traditional & High Performance Materials in Harsh Environment, https://www.researchgate.net/ publication/322211405 Building Material from Calcium Silicate Preparation and Properties, 2010.

[7] Wang, W., Zheng, Q., *Calcium silicate based high efficiency thermal insulation*, British Ceramic Transactions, Vol.99, Issue 4, https://doi.org/10.1179/096797800680 929, 2000.

[8] https://theconstructor.org/building/calcium-silicate-bricks-masonry-construction/17256/

[9] https://insulation.org/io/articles/insulation-materials-calcium-silicate-block-and-pipe/

[10] Hall, M.R., *Materials for energy efficiency and thermal comfort in buildings*, 1st Edition, Elsevier, Ebook ISBN: 9781845699277, 2010.

[11] Munteanu, I.-R., Szava, I., Galfi, P.B., Ambrus, C., Orban, P., *Solutions for improving the load-bearing capacity of resistance structures in case of fires*, 14th Int. Conf. – multidisciplinary, professor Dorin Pavel – the founder of romanian hydropower, https://stiintasiinginerie.ro/wp-content/uploads/2014/07/25-86.pdf, 2014.

[12] Xianyou, Z., Hong, Z.X., 2002, *Study on the properties of the wollastonite short fiber-pvc cable insulation composition*, Conference record of the 1996 IEEE International Symposium on Electrical Insulation, vol.2, 712-715, IEEE xplore, https://doi.org/ 10.1109/ elinsl.1996. 549444, 2002.

[13] https://www.redseal.com/blog/2021/1/19/ how-calcium-silicate-insulates.

[14] https://www.luyangwool.com/search/ calci um % 20silicate.html.

[15] Prati, C., Gandolfi, M.G., *Calcium silicate bioactive cements: biological perspectives and clinical applications*, Dent Mater., 31 (4): 351-370, https://doi.org/10.1016/j.dental. 2016.01.004, 2015.

[16] Persson, C., Engqvist, H., *Premixed calcium silicate for endodontic applications: injectability, setting time and radiopacity*, Biomatter 1 (1): 76-80, https://doi.org/ 10.4161/biom.1.1.16735.

[17] Atmeh, A.R., Chong, E.Z., Richard, G., Festy, F., Watson, T.F., *Dentin-cement interfacial interaction: calcium silicates and polyalkenoates*, J Dent Res. 91 (5): 454-459, https://doi.org/ 10.1177/0022034512443068, 2012.

[18] Shirazi, F.S., Mehrali, M., Oshkour, A.A., Metselaar, H.S., Kadri, N.A., Abu Osman, N.A., *Mechanical and physical properties of calcium silicate/alumina composite for biomedical engineering applications*, J Mech Behav Biomed Mater, 30:168-175, https://doi.org/j.jmbbm. 2013.10.024, 2014.

[19] Zordan-Bronzel, C.L., Esteves Torres, F.F., Tanomaru-Filho, M., Chavez-Andrade, G.M., Bosso-Martelo, R., Guerreiro-Tanomaru, J.M., *Evaluation of physicochemical properties of a new calcium silicate-based sealer, Bio-C Sealer*, J. Endod., 45(10): 1248-1252, https://doi.org/j.joen.2019.07.006, 2019.

[20] Shahi, S., Fakhri, E., Dizaj, S.M., Salatin, S., Sharifi, S., Rahimi, S., *Portland cement: an overview as a root repair material: applications and various modifications*, The Open Dentistry Journal, 16(1), https://doi.org/10.2174/18742106-v16-e221212-2022-54, 2022.

[21] De Almeida, M.S., De Oliveira Fernandes, G.V., De Oliveira, A.M., Granjeiro, J.M., *Calcium silicate as a graft material for bone fractures: a systematic review*, J Int Med Res, 46(7): 2537-2548, https://doi.org/10.1177/ 0300060518770940, 2018.

[22] Wang, G.C., Lu, Z.F., Zreiqat, H., *8 – bioceramics for skeletal bone regeneration*, Bone Substituite Biomaterials, 180-186, https://doi.org/10.1533/9780857099037.2.18 0, 2014.

[23] Wei, K., Peng., Y., Qu, Z., Zhou, H., Pei, Y., Fang, D., *Lightweight composite lattice cylindrical shells with novel character of taylorable thermal expansion*, International Journal of Mechanical Sciences 137, 77-85, https://doi.org/10.1016/j.ijmecsci.2018.01.01 7, 2018.

Received: 25.08.24; **Similarities**: 24.11.24: **Reviewed**: 05.11./07.11.24: **Accepted**:25.11.24.

[24] Toropova, M.M., Steeves, C.A., *Adaptive bimaterial lattices to mitigate thermal expansion mismatch stresses in satelluite structures*, Acta Astronautica 113, 132-141, http://dx.doi.org/10.1016/j.actaastro.2015.03 .022, 2015.

[25] Drebushchak, V.A., *Thermal expansion of solids: review on theories*, Journal of Thermal Analysis and Calorimetry, 142:1097-1113, https://doi.org/10.1007/ s109 73 -020-09370-y, 2020.

[26] Morgan, W.C., *Thermal expansion coefficients of graphite crystals*, Carbon, Vol.10, 73-79, Pergamon Press, 1972.

[27] Pluta, Z., Hryniewicz, T., *Thermal expansion of solids*, Journal of Modern Physics, 3, 793-802, http://dx.doi.org /10.4236/jmp.2012.38104, 2012.

[28] Wang, H., Webb, T., Bitler, J.W., *Study of thermal expansion and thermal conductivity of cemented WC-Co composite*, International Journal of Refractory Metals and Hard Materials 49, 170 – 177, http://dx.doi.org /10.1016/j.ijrmhm.2014.06.009, 2015.

[29] Serway, R.A., Jewett, J.W., *Physics for scientists and engineers book*, 6th edition Thomson Brooks/Cole, p.586, Chapter 19, 2004.

[30] Johnson, R.R., Kural, M.H., Mackey, G.B., *Thermal expansion properties of composite materials*, NASA Contractor Report 165632.

[31] Klemens, P.G., *Thermal expansion of composites*, International Journal of Thermophysics, Vol.7, No.1, Plenum Publishing Corporation, 1986.

[32] Klemens, P.G., *Thermal expansion of composites*, International Journal of Thermophysics, Vol.9, No.2, Plenum Publishing Corporation, 1988.

[33] Jang, J.-S., Varischetti, J., Lee, G.W., Suhr, J., *Experimental and analytical investigation of mechanical damping and CTE of both SiO_2 particle and carbon nanofiber reinforced hybrid epoxy composites*, Composites: Part A 42, 98-103, https://doi.org/10.1016/j.compositesa.2010.1 0.008, 2011.

[34] Lincoln, D.M., Vaia, R.A., Beown, J.M., Benson Tolle, T.H., *Revolutionary nanocomposite materials to enable space systems in the 21st century*, IEEE Aerospace Conference Proceedings, 4, 183-192, https://doi.org/10.1109/AERO.2000.878401, 2000.

[35] Pradere, C., Sauder, C., *Transverse and longitudinal coefficient of thermal expansion of carbon fibers temperatures (300-2500 K)*, Carbon 46, 1874 - 1884, https://doi.org/ 10.1016/j.carbon. 2008.07.035, 2008.

[36] Das, D., Jacobs, T., Barbour, L., *Exceptionally large positive and negative anisotropic thermal expansion of an organic crystalline material*, Nature Mater., 9, 36–39, https://doi.org/10.1038/ nmat2583, 2010.

[37] Wei, K,, Peng, Y., Wang, K., Duan, S., Yang, X., Wen, W., *Three dimensional lightweight lattice structures with large positive, zero and negative thermal expansion*, Composite Structures 188, 287 – 296, https://doi.org/10.1016/j.compstruct. 2018.01.030, 2018.

[38] Xu, H., Farag, A., Pasini, D., *Multilevel hierarchy in bi-material lattices with high specific stiffness and unbounded thermal expansion*, Acta Materialia 137, 155 – 166, http://dx.doi.org/ 10.1016/ j.actamat. 2017 .05 .059, 2017.

[39] Takenaka, K., *Negative thermal expansion materials: technological key for control of thermal expansion*, Sci. Technol. Adv. Mater. 13, 013001, https://doi.org /10.1088/1468-6996/13/0/013001, 2012.

[40] Evans, J.S.O., *Negative thermal expansion materials*, J.Chem.Soc., Dalton Trans., 3317 – 3326, 1999.

[41] Ai, L., Gao, X.-L., *Metamaterials with negative Poisson's ratio and non – positive thermal expansion*, Composite Structures 162, 70 – 84, http://dx.doi.org/10.1016/ j.compstruct. 2016.11.056, 2017.

[42] Shirasu, K., Yamamoto, G., Tamaki, I., Ogasawara, T., Shimamura, Y., Inoue, Y., Hashida, T., *Negative axial thermal expansion coefficient of carbon nanotubes: Experimental determination based on measurements of coefficient of thermal expansion for aligned carbon nanotube reinforced epoxy composites*, Carbon, 95, 904 – 909, http://dx.doi.org/10.1016/ j.carbon.2015.09.026, 2015.

[43] Takezawa, A., Kobashi, M., *Design methodology for porous composites with tunable thermal expansion produced by*

multi-material topology optimisation and additive manufacturing, Composites, Part B 131, 21-29, http://dx.doi.org/10.1016/ j.compositesb.2017.07.054, 2017.

[44] Loser, R., Munch, B., Lura, P., *A volumetric technique for measuring the coefficient of thermal expansion of hardening paste and mortar*, Cement and Concrete Research 40, 1138-117, http://dx.doi.org/10.1016/j.cemconres.2010. 03.021, 2010.

[45] Loukili, A., Chopin, A., Khelidj, A., Le Touzo, J.-Y., *A new approach to determine autogenous shrinkage of mortar at an early age considering temperature history*, Cement and Concrete Research 30, 915-922, 2000.

[46] Wiesner, V.L., Bansal, N.P., *Mechanical and thermal properties of calcium-magnesium aluminosilicate (CMAS) glass*, Journal of the European Ceramic Society 35, 2907-2914, http://dx.doi.org/10.1016/ j.jeurceramsoc.2015.03.032, 2015.

[47] Watanabe, H., Yamada, N., Okaji, M., *Linear thermal expansion coefficient of silicon from 293 to 1000 K*, International Journal of Thermophysics, Vol.25, No.1, 2004.

[48] Enya, K., Yamada, N., Onaka, T., Nakagawa, T., Kaneda, H., Hirabayashi, M., Toulemont, Y., Castel, D., Kanai, Y., Fujishiro, N., *High-precision CTE measurement of SiC-100 for cryogenic space telescopes*, Publications of the Astronomical Society of the Pacific 119, 583-589, 2007.

[49] Ravi, V., Firdosy, S., Caillat, T., Brandon, E., Van Der Walde, K., Maricic, L., Sayir, A., *Thermal expansion studies of selected high-temperature thermoelectric materials*, Journal of Electronic Materials, Vol.38, No.7, http://dx.doi.org/10.1007/s11664-009-0734-2, 2009.

[50] Akikubo, K., Kurahashi, T., Kawaguchi, S., Tachibana, M., *Thermal expansion measurements of nano-graphite using high-temperature X-ray diffraction*, Carbon 169, 307-311, https://doi.org/10.1016/ j.carbon. 2020.07.027, 2020.

[51] Kerstan, M., Muller, M., Russel, C., *Binary, ternary and quaternary silicates of CaO, BaO and ZnO in high thermal expansion seals for solid oxide fuel cells studied by high-temperature X-ray diffraction (HT-XRD)*, Materials Research Bulletin 46, 2456-2463, https://doi.org/ 10.1016/j.materresbull.2011.08.031, 2011.

[52] Aleem, S.A.E., Heikal, M., Morsi, W.M., *Hydration characteristic, thermal expansion and microstructure of cement containing nano-silica*, Construction and Building Materials 59, 151-160, http://dx.doi. org/10.1016/j.conbuildmat.2014.14.02.039, 2014.

[53] Yeon, J.H.; Choi, S.; Won, M.C., *In situ measurement of coefficient of thermal expansion in hardening concrete and its effect on thermal stress development*, Construction and Building Materials 38, 306-315, http://dx.doi.org/10.1016/j. conbuildmat.2012.07.111, 2013.

[54] di Scalea, F.L., *Measurement of thermal expansion coefficients of composites using strain gages*, Experimental Mechanics, Vol.38, No.4, 233-241, 1998.

[55] Niu, Y., Wang, J., Shao, S., Wang, H., Lee, H., Park, S.B., *A comprehensive solution for electronic package's reliability assessment with digital image correlation (DIC) method*, Microelectronics Reliability 87, 81-88, https://doi.org/10.1016/j. microrel.2018.06.006, 2018.

[56] Hoult, N.A., Take, W.A., Lee, C., Dutton, M., *Experimental accuracy of two dimensional strain measurements using digital image correlation*, Engineering Structures 46, 718-726, http://dx.doi.org/ 10.1016/j.engstruct.2012.08.018, 2013.

[57] Bing, P., Hui-min, X., Tao, H., Asundi, A., *Measurement of coefficient of thermal expansion of films using digital image correlation method*, Polymer Testing 28, 75-83, 2009.

[58] Mendes, S.S., Filho, J.C.A.D., Melo, A.R.A., Nunes, L.C.S., *Determination of thermal expansion coefficient of a monofilament polyamide fiber using digital image correlation*, Polymer Testing 87, 106540, https://doi.org/10.1016/j.poly mertesting.2020.106540, 2020.

[59] Graciani, E., Justo, J., Zumaquero, P.L., *Determination of in-plane and through-the-*

Received: 25.08.24; **Similarities**: 24.11.24: **Reviewed**: 05.11./07.11.24: **Accepted**:25.11.24.

thickness coefficients of thermal expansion in composite angle brackets using digital image correlation, Composite Structures 238, 111939, https://doi.org/10.1016 /j.compstruct.220.111939, 2020.

[60] Botean, A.I., *Thermal expansion coefficient determination of polylactic acid using digital image correlation*, E3S Web of Conferences 32, 01007, https://doi.org /10.1051/e3sconf/20183201007, 2018.

[61] Herbst, C., Splitthof K., *Q400 Application Note - T-Q400-Basics-3DCORR-002a-EN*, Dantec Dynamics GmbH, Germany, www.dantecdynamics.com, 2006.

[62] Sciammarella, C.A., Sciammarella, F.M., *Experimental Mechanics of Solids*, John Wiley & Sons, 2012.

[63] Becker, T., Splitthof, K., Siebert, T., Kletting, P., *Error Estimations of 3D Digital Image Correlation Measurements*, Proceedings of SPIE, 634, art. no. 63410F, 2006.

[64] Siebert, T., Becker, T., Spiltthof, K., Neumann, I., Krupka, R., *Error estimations in digital image correlation technique*, Applied Mechanics and Materials, vol. 7-8, p.265-270, 2007.

ANALIZA COEFICIENTULUI DE DILATARE TERMICĂ A SOLIDELOR ANIZOTROPE: APLICARE LA SILICATUL DE CALCIU – PARTEA I – INTRODUCERE ÎN METODOLOGIA DE MĂSURARE

Rezumat. Această lucrare se propune determinarea coeficientului de dilatare termică liniară (CTE) pentru silicatul de calciu utilizând o metodă optică de măsurare a deformațiilor numită metoda de corelare a imaginii digitale (DIC). DIC furnizează câmpuri de deformare, în plan, a întregii suprafețe a probei plane analizate, prin compararea imaginilor digitale ale suprafeței specimenului obținute înainte și după deformare. Probele evaluate în această lucrare sunt două plăci de silicat de calciu: una pătrată (cu laturile de 50x50 mm și 3 mm grosime) și una circulară (cu un diametru de 50 mm și o grosime de 3 mm). Standul de măsurare dezvoltat include un dispozitiv de încălzire, senzori termici și o termo-cameră pentru măsurarea și monitorizarea în timp real a temperaturii probei precum și un sistem de măsurare 2D și 3D-DIC a deformaţiilor. Studiul se efectuează pe parcursul a două etape: Partea I – Introducerea în metodologia de măsurare şi Partea II – Evaluarea datelor experimentale.

Adrian-Ioan BOTEAN, Lecturer, PhD.Eng., Mechanical Engineering Department, Faculty of Automotive, Mechatronics and Mechanics, Technical University of Cluj-Napoca, 28 Memorandumului, 400114 Cluj-Napoca, Romania; adrian.ioan.botean@rezi.utcluj.ro